# 2D Forward Looking SONAR in Underwater Navigation Aiding: an AUKF-based strategy for AUVs *

**Matteo Franchi** *,** **Alessandro Ridolfi** *,**
**Leonardo Zacchini** *,**

* Department of Industrial Engineering, University of Florence,
via di Santa Marta 3, 50139, Florence, Italy (e-mail:
matteo.franchi@unifi.it).
** Interuniversity Center of Integrated Systems for the Marine
Environment (ISME), www.isme.unige.it

**Abstract:** This paper proposes an underwater navigation system where linear speed estimations, obtained with a 2D Forward-Looking SONAR (FLS), are integrated within a navigation filter and this solution is shown to work satisfyingly in the absence of Doppler Velocity Log (DVL) readings. Both to provide a better description of the system, which is a dynamic entity in a dynamic environment and to characterize FLS measurements, an Adaptive Unscented Kalman Filter (AUKF)-based estimator is here proposed. The solution has been tested and validated offline making use of navigation data obtained during sea trials performed in July 2018 with FeelHippo AUV at the basin of the NATO Science and Technology Organization Centre for Maritime Research and Experimentation (CMRE), La Spezia (Italy).

*Keywords:* Autonomous underwater vehicles, marine system navigation, guidance and control, mechatronic systems, data-fusion, nonlinear observers and filter design, Kalman filtering techniques in marine systems control, perception and sensing, field robotics.

## 1. INTRODUCTION

Most of the underwater navigation systems are based on the Kalman Filter (KF) (Kalman, 1960) or its variants to nonlinear systems such as the Extended Kalman Filter (EKF) (Bar-Shalom et al., 2004), or the Unscented Kalman Filter (UKF) (Allotta et al., 2015) where, most of the times, the linear speed of the Autonomous Underwater Vehicle (AUV) is retrieved using the Doppler Velocity Log (DVL).

An Adaptive Unscented Kalman Filter (AUKF)-based solution with Forward-Looking SONAR (FLS) measurements to aid underwater navigation is here proposed and it is shown to work satisfyingly without exploiting DVL readings. Nevertheless, it is worth stressing that cooperation with the DVL is possible, this way obtaining more linear speed measurements. In the following, the here proposed solution is tested in the worst-case scenario, so any readings from the DVL is employed. Navigation-aiding using an FLS could outline several advantages. Indeed, employing an augmented set of devices for navigation purposes represents a boost in redundancy and, in addition to this, multitasking on-board sensors represent a solution that avoids the use of some instruments and offers compactness (*e.g.*, thinking about small marine robots).

It is well known that the KF is an optimal estimator in the Minimum Mean Square Error (MMSE) sense under linear Gaussian assumptions (Bar-Shalom et al., 2004). However, generally speaking, the optimality of Bayesian state estimators depends on the quality of the process noise and measurement noise statistics. In practical situations, they are either unknown or approximately known and, therefore, often tuned and adjusted while performing the estimation. Poor knowledge of the a priori statistics will either worsen the precision of the estimator (producing unwanted estimation errors) (Obsharsky et al., 1969) or cause the divergence of the filter (Mehra, 1972). To overcome the above-mentioned issues, researches often relied on the Adaptive Kalman Filter (AKF) (Mohamed and Schwarz, 1999) or its variants applied to EKF (Jetto et al., 1999) or UKF (Soken and Hajiyev, 2012). Adaptive techniques intrinsically place less reliance on the a priori information and the problem of unknown or approximately known noise statistics is solved by continuously exploiting the filter learning history. In addition to this, having a dynamic adaptation that evolves in a dynamic environment usually leads to better performance (Mohamed and Schwarz, 1999).

Moreover, employing *registration* methods [1] to FLS images poses relevant issues on measurement noise description. Some authors, such as (Pfingsthorn et al., 2010) and (Hurtós et al., 2015), proposed heuristic methods based on metrics calculated during the *registration* process. How-

[1] *Registration* is intended as the process through which a pair of overlapped images that insonify a common region are related each other.

ever, this way of thinking is prone to provide, according to the metrics employed, different results. To obtain a more sophisticated, reliable and dynamic description of the system and to characterize FLS measurements, an AUKF estimator is then here proposed. Indeed, with regards to FLS noise description, adaptive methods intrinsically solve the problem of unknown noise characterization by continuously exploiting current and past measurements and estimations. As a consequence, even if the *registration* process can be deemed as successful basing on some metrics calculated during the *registration* step, its uncertainty is adaptively computed by the navigation filter. For what concerns UKFs, AUKF-based proposals can be found for example in (Sun et al., 2011), (Hajiyev and Soken, 2014), (Gao et al., 2015), and (Zheng et al., 2018), whereas marine robotics applications, which involve a standard inertial navigation sensor set (any FLS employed), are very limited and few contributions can be found for example in (Zhu et al., 2009) where only simulations are presented, in (Mehrjouyan and Alfi, 2019) where data obtained during sea trials are post-processed and in (Davari and Gholami, 2016) where experimental tests conducted on a vessel are presented. To the authors' best knowledge, adaptive filtering in the marine field has not been completely tackled yet and it is still a niche and open problem. Although the mathematical and theoretical foundations have been widely investigated since the '70s, applications to underwater navigation are very limited.

The solution has been tested and validated offline making use of navigation data obtained during the European Robotics League/Student Autonomous Underwater Vehicles Challenge 2018 (ERL/SAUC-E 2018) competition (Ferri et al., 2017), held in La Spezia (Italy) at the NATO Science and Technology Organization Centre for Maritime Research and Experimentation (CMRE) in July 2018 with FeelHippo AUV, an autonomous vehicle developed by the Department of Industrial Engineering of the University of Florence (UNIFI DIEF).

The remainder of the paper is organized as follows: Section 2 is dedicated to preliminaries, whereas Section 3 addresses the mechanical design and the hardware architecture of FeelHippo AUV. Section 4 treats the proposed navigation strategy, whereas Section 5 describes the offline tests. Finally, Section 6 draws conclusions.

## 2. PRELIMINARIES AND NOTATION

This chapter covers the notation employed in the rest of the work and gives a complete review of the fundamental theoretical and mathematical concepts used throughout this contribution. The kinematic and dynamic modeling of an AUV is treated in Section 2.2, whereas the main concepts about linear speed estimations with an FLS are discussed in Section 2.1.

The pose of the AUV is described with respect to two reference frames. The first one is a local Earth-fixed reference frame whose axes point, respectively, North, East, and Down (*NED frame*) $\{O^N x^N y^N z^N\}$, whereas the second one is centered on the Center of Gravity (CG) of the vehicle with the forward motion direction represented by the x-axis (*surge*) and the z-axis (*heave*) pointing down. Lastly, the y-axis (*sway*) completes a right-handed reference frame $\{O^b x^b y^b z^b\}$ (*body frame*). In addition to this, a reference frame centered on the FLS center with the

x-axis pointing forward, the z-axis pointing down and the y-axis in accordance with a right-handed reference frame $\{O^{FLS} x^{FLS} y^{FLS} z^{FLS}\}$, is considered.

### 2.1 2D FLS imaging model and phase correlation technique for speed estimation

The acoustic insonification of the scene can be described using three parameters: the azimuth angle ($\alpha$), the elevation angle ($\beta$), and the delivering range ($R_\rightarrow$), see Fig.1 and (Franchi et al., 2019) for further information. According to the authors' previous works (Franchi et al.,
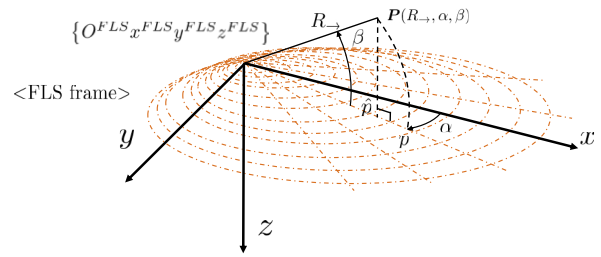


Fig. 1. FLS imaging model.

2018) and (Franchi et al., 2019), the nonlinear model that projects a generic 3D point $\boldsymbol{P}$ onto the image plane ($p$ in Fig.1) can be simplified, under the hypotheses of small tilt angle (for the mounting configuration) and small elevation angle, to a 2D approximated model (*orthographic projection model*, see $\hat{p}$ in Fig.1). It is worth stressing that the two conditions above are usually met; indeed, a small tilt angle permits to insonify wider areas (and so it is a largely employed configuration), whereas the elevation angle is typically around 7°-10° for most FLS devices. In such a situation, neglecting roll and pitch variations (if roll and pitch variations are consistent, a tilt unit can be employed to maintain the FLS to an approximately desired configuration), two different FLS views are related through a plane roto-translation (3-parameter Euclidean transformation), and thus phase correlation methods can be suitably employed for image *registration* (Hurtós et al., 2015) and (Ferreira et al., 2015).

The key concept of phase correlation is based on the so-called Fourier shift property. In fact, in the Fourier domain, a shift between two images appears as a linear phase shift. Given two images $i_{t_1}(x,y)$ and $i_{t_2}(x,y)$ translated of a quantity $\boldsymbol{s} = \begin{bmatrix} s_x & s_y \end{bmatrix}^T \in \mathbb{R}^2$ (1), where the subscript indicates the absolute acquisition time, $\boldsymbol{s}$ is the translation on the image plane and $t_1 < t_2$, it can be shown (De Castro and Morandi, 1987), (Hurtós et al., 2015) and (Franchi et al., 2019) that $\boldsymbol{s}$ can be obtained from the location of the peak of the cross-power spectrum (2), (3), and (4).

$$i_{t_1}(x,y) = i_{t_2}(x - s_x, y - s_y), \tag{1}$$

$$C(m,n) = \frac{I_{t_1}(m,n) I_{t_2}^*(m,n)}{\left| I_{t_1}(m,n) I_{t_2}^*(m,n) \right|} = e^{-j2\pi(m s_x + n s_y)}, \tag{2}$$

$$c(x,y) = \mathcal{F}^{-1}\{C(m,n)\} \tag{3}$$

$$\boldsymbol{s} = \begin{bmatrix} s_x \\ s_y \end{bmatrix} = \arg\max_{(x,y)}\{c(x,y)\} \tag{4}$$

where $I_{t_1}$ and $I_{t_2}$ are the Fourier Transform (FT) of $i_{t_1}$ and $i_{t_2}$ respectively, $C(m,n)$ is the cross-power spectrum in the

frequency domain, $c(x, y)$ is the cross-power spectrum in the spatial domain, $\mathcal{F}^{-1}$ is the inverse FT operator, and $*$ denotes the complex conjugate. By taking advantage of a linear transformation that considers the maximum range of the FLS and the dimension of the FLS images, $\boldsymbol{s}$ is mapped from *pixel* to *meters* (or another similar physical quantity). Afterward, the speed estimation can be computed by using the arrival time of the FLS images. See (Franchi et al., 2020) for more information.

### 2.2 Kinematic and dynamic modeling of the AUV

The AUV pose with respect to the *NED frame* is indicated with $\boldsymbol{\eta} = \begin{bmatrix} \boldsymbol{\eta}_1^T & \boldsymbol{\eta}_2^T \end{bmatrix}^T \in \mathbb{R}^6$, where $\boldsymbol{\eta}_1$ is the position of the CG of the vehicle with respect to the *NED frame* and $\boldsymbol{\eta}_2$ its orientation; here, a triplet of Euler angles expressed with respect to the *NED frame*, namely Roll ($\phi$), Pitch ($\theta$), and Yaw ($\psi$), is used (RPY). The linear and angular velocities of the vehicle with respect to the *body frame* reference frame are denoted with $\boldsymbol{\nu} = \begin{bmatrix} \boldsymbol{\nu}_1^T & \boldsymbol{\nu}_2^T \end{bmatrix}^T$. The *NED frame* and the *body frame* are visible in Fig.2. The
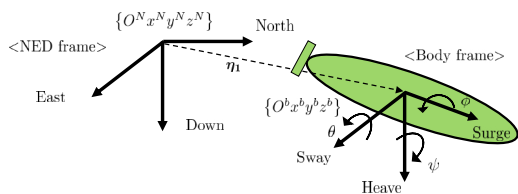


Fig. 2. *NED frame* and *body frame* representation.

kinematic model is reported in (5). For more information the interested reader can refer to (Fossen et al., 1994).

$$\begin{pmatrix} \dot{\boldsymbol{\eta}}_1 \\ \dot{\boldsymbol{\eta}}_2 \end{pmatrix} = \begin{bmatrix} R_b^N(\boldsymbol{\eta}_2) & 0_{3\times 3} \\ 0_{3\times 3} & T_b^N(\boldsymbol{\eta}_2) \end{bmatrix} \begin{pmatrix} \boldsymbol{\nu}_1 \\ \boldsymbol{\nu}_2 \end{pmatrix}, \qquad (5)$$

where $R_b^N$ is the rotation matrix between the body and the fixed reference system and $T_b^N(\boldsymbol{\eta}_2)$ represents the Euler matrix. With regard to the dynamic modeling of the AUV, the classic description of (Fossen et al., 1994), reported in (6) is employed.

$$M_m \dot{\boldsymbol{\nu}} + C(\boldsymbol{\nu})\boldsymbol{\nu} + D(\boldsymbol{\nu})\boldsymbol{\nu} + \boldsymbol{g}_{\boldsymbol{\eta}}(\boldsymbol{\eta}) = \boldsymbol{\tau}(\boldsymbol{\nu}, \boldsymbol{u}_{rpm}), \qquad (6)$$

where $M_m$ is the mass matrix, $C(\boldsymbol{\nu})$ is the centripetal and Coriolis matrix, $D(\boldsymbol{\nu})$ is the damping matrix, $\boldsymbol{g}_{\boldsymbol{\eta}}(\boldsymbol{\eta})$ takes into account the effects of gravity and buoyancy, and $\boldsymbol{\tau}(\boldsymbol{\nu}, \boldsymbol{u}_{rpm})$ describes the map between the vehicle speed ($\boldsymbol{\nu}$) and the rotational speed of the motors ($\boldsymbol{u}_{rpm}$) to the resultant thrust action on the vehicle. Equation (6) can be simplified exploiting the following assumptions:

- the longitudinal motion only is considered for the AUV. Indeed, the longitudinal direction is that of minimal drag. Therefore, most of the underwater missions are performed along the longitudinal direction;
- the mass matrix is considered as diagonal;
- given the low speed involved, the coupling between the dissipative effects are neglected;
- added masses are neglected, gravitational, centripetal, and Coriolis effects are not considered.

The above-mentioned assumptions are similar to those already exploited by the authors (Franchi et al., 2020).

In light of the above-mentioned assumptions, the AUV dynamics can be represented as in (7).

$$m\dot{\nu}_{1x} = \tau_{1x}(\boldsymbol{\nu}, \boldsymbol{u}) - \delta_x \nu_{1x}^2 \operatorname{sgn}(\nu_{1x}), \qquad (7)$$

where $m$ is the dry mass of the vehicle, $\tau_{1x}(\boldsymbol{\nu}, \boldsymbol{u})$ is the component of $\boldsymbol{\tau}$ along the *surge* axis of the AUV, $\nu_{1x}$ is the component of $\boldsymbol{\nu}$ along the *surge* axis of the AUV, and $\delta_x$ represents the coefficient for the longitudinal drag. The adopted propulsion model (namely the relation $\tau_{1x}(\boldsymbol{\nu}, \boldsymbol{u})$) is described by the authors in (Allotta et al., 2016b) and (Franchi et al., 2020), whereas $\delta_x$ has been estimated by applying a Least Squares (LS) technique and for further information the interested reader can refer to (Allotta et al., 2018).

## 3. FEELHIPPO AUV DESCRIPTION

FeelHippo AUV has been designed and developed by the UNIFI DIEF both for the participation in student robotics competitions and for undertaking research topics. From the first low-budget prototype to the final version, Feel-Hippo AUV has been substantially changed over the years and its current version, which is described in the following, is visible in Fig.3. FeelHippo AUV reduced dimensions and
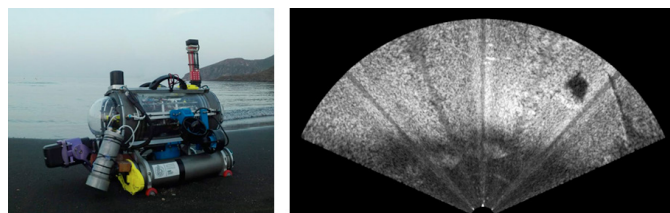


Fig. 3. On the left, FeelHippo AUV, whereas on the right, an image obtained with the FLS.

weight leads to a compact underwater platform and, in addition to this, the presence of top-of-the-line sensors makes FeelHippo AUV capable of undertaking complex tasks and missions. The main physical features are reported in table 1. A list of all the electronic devices and the sensors with

Table 1. FeelHippo AUV physical data and performance.

| FeelHippo AUV main characteristics | |
|---|---|
| Dimensions [mm] | approx. $600\times 640\times 500$ |
| Dry mass [kg] | 35 |
| $\delta_x$ [N/s²m²] | 65 |
| Max longitudinal speed [m/s] (kn) | approx. 1 (2) |
| Max lateral speed [m/s] (kn) | approx. 0.2 (0.4) |
| Max depth [m] | 30 |
| Autonomy [h] | 2-3 |

which FeelHippo AUV is equipped is here listed:

- Intel i-7-based LP-175-Commel motherboard (used for onboard processing);
- U-blox 7P precision Global Positioning System (GPS);
- Orientus Advanced Navigation Attitude Heading Reference System (AHRS);
- KVH DSP 1760 single-axis high precision Fiber Optic Gyroscope (FOG);
- Nortek DVL1000 DVL, measuring linear velocity and acting as Depth Sensor (DS);
- EvoLogics S2CR 18/34 acoustic modem;

- Teledyne BlueView M900 2D FLS;
- Ubiquiti Bullet M2 WiFi access point;
- 868+ RFDesign radio modem;
- one bottom-looking ELP 720p MINI IP camera;
- one Microsoft Lifecam Cinema forward-looking camera;
- two lateral ELP 1080p MINI IP cameras;
- two Intel Neural Compute Stick 2 for Artificial Intelligence (AI) applications.

## 4. PROPOSED SOLUTION

The navigation filter employs a parallel structure to obtain an accurate estimate of the pose of the AUV. In particular, attitude is independently estimated from the position and its output represents an input for the position estimation filter. More information can be found in (Allotta et al., 2016a).

In the following, the AUKF filter for position estimation, which is the proposed contribution, is described. The behavior of the AUV is described with the following state variables:

$$\boldsymbol{x} = [\,\boldsymbol{\eta}_1^T\ \boldsymbol{\nu}_1^T\,]^T, \tag{8}$$

with $\boldsymbol{x} \in \mathbb{R}^6$. In light of the discussion presented in Section 2.2, the model employed for the evolution of the state is given in (9).

$$
\begin{bmatrix} \boldsymbol{\eta}_1 \\ \boldsymbol{\nu}_1 \end{bmatrix}_k = \begin{bmatrix} \boldsymbol{\eta}_1 \\ \boldsymbol{\nu}_1 \end{bmatrix}_{k-1} +
$$
$$
\Delta T \begin{bmatrix} R_B^N \left((\boldsymbol{\eta}_2)_{k-1}\right)(\boldsymbol{\nu}_1)_{k-1} \\ \frac{\tau_{1,x}(\boldsymbol{\nu}_{k-1},\boldsymbol{u}_{k-1})}{m} - \frac{(\delta_x)_{k-1}\nu_{1x}^2\,\mathrm{sgn}(\nu_{1x})}{m} \\ 0 \\ 0 \end{bmatrix} + \boldsymbol{w}_{k-1}, \tag{9}
$$

where $\Delta T$ is the sampling time. The measurement vector is:

$$\boldsymbol{y}_k = \left[(\boldsymbol{P}_{GPS})^T\, d_{DS}\, (\boldsymbol{v}_{FLS})^T\right]_k^T, \tag{10}$$

where $\boldsymbol{P}_{GPS}$ is the GPS measurement, $d_{DS}$ is the DS reading, and $\boldsymbol{v}_{FLS}$ is the speed estimated with the FLS. Therefore, the measurement equation becomes (11).

$$\boldsymbol{y}_k = H_k \boldsymbol{x}_k + \boldsymbol{v}_k, \tag{11}$$

where it is easy to understand that $H_k$ is a matrix that contains 0 or 1. $\boldsymbol{w}$ and $\boldsymbol{v}$ are modeled as zero mean stationary white noise and initial state and process and measurement noises are assumed to have zero cross-correlation, $E\left[\boldsymbol{w}_{k-1}\boldsymbol{w}_{k-1}^T\right] = Q_{k-1}$ is the process noise covariance matrix, and $E\left[\boldsymbol{v}_k\boldsymbol{v}_k^T\right] = R_k$ is the measurement noise covariance matrix.

The *residual* vector is defined as $\boldsymbol{v}_k = \boldsymbol{y}_k - \boldsymbol{h}_k(\boldsymbol{x}_{k|k})$ and the *innovation* vector is $\boldsymbol{\mu}_k = \boldsymbol{y}_k - \boldsymbol{h}_k(\boldsymbol{x}_{k|k-1})$, where the notation $_{j|k}$ stands for "at iteration $j$ given information up to the $k$-th iteration".

### 4.1 Adaptive estimation of R

With regard to the estimation of the matrix $R$, under the hypotheses of the classic linear KF, (Mohamed and Schwarz, 1999) shown that an estimate of $R$ at the instant $k$ can be obtained, exploiting the residual $\boldsymbol{v}_k$:

$$\hat{R}_k = \frac{1}{N_{R_w}} \sum_{i=i_0}^{k} \boldsymbol{v}_i \boldsymbol{v}_i^T + H_k P_{k|k} H_k^T, \tag{12}$$

where $P$ is the state covariance, $\hat{\bullet}$ denotes an estimate, $i_0 = k - N_{R_w} + 1$, and $N_{R_w} \in \mathbf{N}^+$ is the size of the moving window. In conclusion, when applied to the UKF, (12) becomes:

$$\hat{R}_k = \frac{1}{N_{R_w}} \sum_{i=i_0}^{k} \boldsymbol{v}_i \boldsymbol{v}_i^T + \sum_{i=0}^{2n_a} W_i^{(c)} (\boldsymbol{\mathcal{H}}_i - \hat{\boldsymbol{y}}_{k|k})(\boldsymbol{\mathcal{H}}_i - \hat{\boldsymbol{y}}_{k|k})^T, \tag{13}$$

where $W_i^{(c)}$ is the i-th weight to compute the mean in the Unscented Transform (UT), $\boldsymbol{\mathcal{H}}_i$ are the $\sigma$-points propagated through the measurement model, and $n_a$ is the state dimension (in this case 6). It is easy to understand that the estimated $\hat{R}_k$ matrix is positive definite.

### 4.2 Adaptive estimation of Q

With regard to the estimation of the matrix $Q$, making use of linearization approximations, it can be shown that $Q_{k-1} = E[\boldsymbol{w}_{k-1}\boldsymbol{w}_{k-1}^T]$ can be approximated with:

$$Q_{k-1} \approx L_k E[\boldsymbol{\mu}_k \boldsymbol{\mu}_k^T] L_k^T, \tag{14}$$

where $L_k$ is the Kalman gain at the instant $k$. $E[\boldsymbol{\mu}_k \boldsymbol{\mu}_k^T]$ is calculated (at the instant $k$) with an average through a moving window of size $N_{Q_w} \in \mathbf{N}^+$.

$$\frac{1}{N_{Q_w}} \sum_{i=i_0}^{k} \boldsymbol{\mu}_i \boldsymbol{\mu}_i^T, \tag{15}$$

where $i_0 = k - N_{Q_w} + 1$.
In conclusion, an estimate of $Q_{k-1}$ is:

$$\hat{Q}_{k-1} = L_k \frac{1}{N_{Q_w}} \sum_{i=i_0}^{k} \boldsymbol{\mu}_i \boldsymbol{\mu}_i^T L_k^T \tag{16}$$

It is easy to understand that the estimated $\hat{Q}_{k-1}$ matrix is positive definite.

### 4.3 Method

The proposed approach is to test if the filter is consistent and if not to apply a suitable adaptation to the prior filter statistics (namely matrix $R$ and $Q$). To this end, the innovation process $\boldsymbol{\mu}_k$ is hypothesized to be well described by a zero-mean white sequence. In such a condition, (17) can be used to test the consistency of the filter (which obviously is necessary for its optimality).

$$(\varphi_\chi)_k = \boldsymbol{\mu}_k^T S_k^{-1} \boldsymbol{\mu}_k, \tag{17}$$

$(\varphi_\chi)_k \in \mathbb{R}$ presents a $\chi_\varsigma^2$ distribution where $\varsigma$ denotes the degrees of freedom (equal to the dimension of the vector $\boldsymbol{\mu}_k$). The following test is well known in the literature as Normalized Innovation Squared (NIS) test, see (Bar-Shalom et al., 2004) for more information.
In particular, if (18) holds, an adaptation of the prior statistics $R$ and/or $Q$ is pursued.

$$(\varphi_\chi)_k > \overline{\chi}_{\varsigma,\varrho}^2, \tag{18}$$

where $\overline{\chi}_{\varsigma,\varrho}^2$ is a scalar that depends upon $\varsigma$ and $\varrho$, where the latter is the reliability level chosen by the designer.
Because of the different sampling rates of the available sensors, the structure of the matrix $H_k$ might change at each iteration. Furthermore, during real tests at sea, FLS-based speed measurements have an unpredictable rate. Indeed, if the sea bottom presents poor informative

content, FLS estimations might not be achieved.

If one or more measurements are not available at the iteration $k$, the corresponding rows of the innovation vectors $\boldsymbol{\mu}_k$ and $\boldsymbol{v}_k$ are replaced with zero. This way only current measurements give a contribution. Consequently, (13) and (16) become (19) and (22) respectively.

$$\hat{R}_k = [\sum_{i=i_0}^{k} \boldsymbol{v}_i^\star \boldsymbol{v}_i^{\star T}] \div [N_{R_w}^\star] + \sum_{i=0}^{2n_a} W_i^{(c)} (\boldsymbol{\mathcal{H}}_i - \hat{\boldsymbol{y}}_{k|k})(\boldsymbol{\mathcal{H}}_i - \hat{\boldsymbol{y}}_{k|k})^T, \tag{19}$$

where $\div$ represents the element-wise division,

$$v_i^{j\star} = \begin{cases} v_i^j & H_i^j \neq 0_{1 \times n_a} \\ 0 & H_i^j = 0_{1 \times n_a} \end{cases} \tag{20}$$

with the superscript is denoted the $j - th$ row of $\boldsymbol{v}_i^\star$.

$$N_{R_w}^\star = \sum_{i=i_0}^{k} \boldsymbol{I}_{yi} \boldsymbol{I}_{yi}^T, \tag{21}$$

where $\boldsymbol{I}_{yi}$ at the instant $i$ is a column vector whose rows are 1 if the corresponding measurement has arrived or 0 otherwise and $k = N_{R_w} + i_0 - 1$.

$$\hat{Q}_{k-1} = L_k \sum_{i=i_0}^{k} [\boldsymbol{\mu}_i^\star \boldsymbol{\mu}_i^{\star T} \div N_{Q_w}^\star] L_k^T, \tag{22}$$

where $\div$ represents the element-wise division,

$$\mu_i^{j\star} = \begin{cases} \mu_i^j & H_i^j \neq 0_{1 \times n_a} \\ 0 & H_i^j = 0_{1 \times n_a} \end{cases} \tag{23}$$

with the superscript is denoted the $j - th$ row of $\boldsymbol{\mu}_i^\star$.

$$N_{Q_w}^\star = \sum_{i=i_0}^{k} \boldsymbol{I}_{yi} \boldsymbol{I}_{yi}^T, \tag{24}$$

where $\boldsymbol{I}_{yi}$ is defined above and $k = N_{Q_w} + i_0 - 1$.

## 5. OFFLINE TESTS

In this section, the navigation data retrieved during an underwater mission performed at the ERL-SAUCE 2018 competition held in La Spezia (Italy) in July 2018 are used. The mission lasted 960 s and it covered approximately 220 m; the desired depth was 2 m (the altitude resulted approximately constant and equal to 2 m too) and the reference longitudinal cruise speed was 0.5 m/s. Moreover, the FLS maximum range was set to 10 m.

A rectangle with the approximate dimensions $36 \times 20$ m was the area of interest. The final results are visible in Fig.4, where the ground-truth navigation is a DVL-based Dead Reckoning (DR) strategy. Furthermore, GPS fixes were acquired before diving and after resurfacing. The metrics defined in (25) and (26) are used to evaluate the proposed solution and the results are depicted in Fig.5 and Fig.6.

$$e_k = \left\| \boldsymbol{\eta}_{1_{GT_k}} - \boldsymbol{\eta}_{1_{PS_k}} \right\| \tag{25}$$

$$\bar{e}_k = \frac{\sum_{i=0}^{i=k} e_i}{k}, \tag{26}$$

where $e_k \in \mathbb{R}^+$ denotes the navigation error at the instant $k$, $\boldsymbol{\eta}_{1_{GT_k}}$ and $\boldsymbol{\eta}_{1_{PS_k}}$ indicate the position of the AUV at the instant $k$ according to the ground-truth and to the proposed solution respectively. $\bar{e}_k \in \mathbb{R}^+$ is the mean of all the computed errors $e_k$.
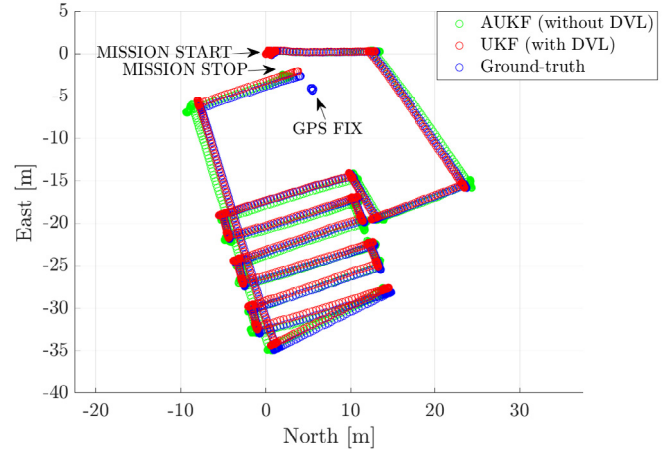


Fig. 4. Navigation results for the AUKF. The proposed solution is in green and the ground-truth path is in blue. "GPS FIX" is the GPS position after resurfacing. The resurfacing error, according to the GPS fixes, is around 3.7 m. In addition, the results using a simple UKF with DVL readings are presented in red.
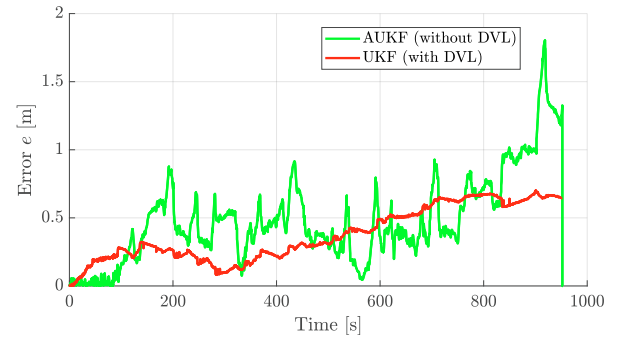


Fig. 5. Error as defined in (25). The jump at the end, around 1000 s, is due to the resurfacing.
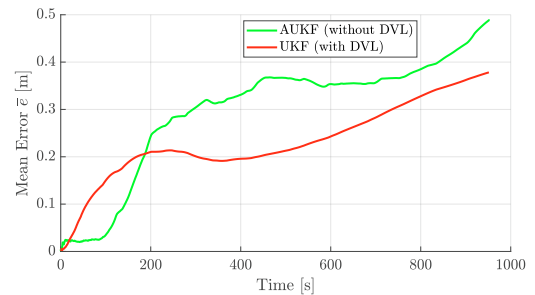


Fig. 6. Error as defined in (26). During underwater operations, due to the lack of absolute position measurements, the error increases over time (remaining below 0.5 m). However, by suitable employing absolute positioning systems, such as Long BaseLine (LBL) and the Ultra-Short BaseLine (USBL), or integrating the proposed navigation system within a Simultaneous Localization And Mapping (SLAM) framework, the error can be bounded.

## 6. CONCLUSION

This work presents an AUKF-based navigation strategy tailored to AUVs where linear speed estimations are ob-

tained making use of a 2D FLS only (cooperation with the DVL is possible anyway). The proposed solution has been tested and validated, showing remarkable results, using data gathered during sea trials undertaken in La Spezia (Italy) at the NATO STO CMRE in July 2018. The final results are encouraging and the navigation error is always maintained below 2 m with respect to a DVL-based DR strategy, whereas the resurfacing error, after about 220 m of navigation, is around 3.7 m.

## REFERENCES

Allotta, B., Caiti, A., Costanzi, R., Fanelli, F., Fenucci, D., Meli, E., and Ridolfi, A. (2016a). A new AUV navigation system exploiting Unscented Kalman Filter. *Ocean Engineering*, 113, 121–132.

Allotta, B., Caiti, A., Chisci, L., Costanzi, R., Di Corato, F., Fantacci, C., Fenucci, D., Meli, E., and Ridolfi, A. (2016b). An Unscented Kalman Filter based navigation algorithm for Autonomous Underwater Vehicles. *Mechatronics*, 39, 185–195.

Allotta, B., Chisci, L., Costanzi, R., Fanelli, F., Fantacci, C., Meli, E., Ridolfi, A., Caiti, A., Di Corato, F., and Fenucci, D. (2015). A comparison between EKF-based and UKF-based navigation algorithms for AUVs localization. In *Proceedings of OCEANS'15 MTS/IEEE GENOVA, Genova (IT)*. IEEE.

Allotta, B., Costanzi, R., Pugi, L., and Ridolfi, A. (2018). Identification of the main hydrodynamic parameters of Typhoon AUV from a reduced experimental dataset. *Ocean Engineering*, 147, 77–88.

Bar-Shalom, Y., Li, X.R., and Kirubarajan, T. (2004). *Estimation with applications to tracking and navigation: theory algorithms and software*. John Wiley & Sons.

Davari, N. and Gholami, A. (2016). An Asynchronous Adaptive Direct Kalman Filter algorithm to improve underwater navigation system performance. *IEEE Sensors Journal*, 17(4), 1061–1068.

De Castro, E. and Morandi, C. (1987). Registration of translated and rotated images using finite Fourier transforms. *IEEE Transactions on Pattern Analysis and Machine Intelligence*, PAMI-9(5), 700–703.

Ferreira, F., Djapic, V., Micheli, M., and Caccia, M. (2015). Forward Looking SONAR mosaicing for mine countermeasures. *Annual Reviews in Control*, 40, 212–226.

Ferri, G., Ferreira, F., and Djapic, V. (2017). Multidomain robotics competitions: The CMRE experience from SAUC-E to the European Robotics League Emergency Robots. In *Proceedings of OCEANS'17 MTS/IEEE ABERDEEN, Aberdeen (UK)*. IEEE.

Fossen, T.I. et al. (1994). *Guidance and control of ocean vehicles*. John Wiley & Sons.

Franchi, M., Ridolfi, A., and Pagliai, M. (2020). A forward-looking SONAR and dynamic model-based AUV navigation strategy: Preliminary validation with Feelhippo AUV. *Ocean Engineering*, 196, 106770.

Franchi, M., Ridolfi, A., and Zacchini, L. (2018). A Forward-Looking SONAR-based system for underwater mosaicing and acoustic odometry. In *2018 IEEE/OES Autonomous Underwater Vehicle Workshop (AUV), Porto (P)*. IEEE.

Franchi, M., Ridolfi, A., Zacchini, L., and Benedetto, A. (2019). Experimental evaluation of a Forward-Looking SONAR-based system for acoustic odometry. In *Proceedings of OCEANS'19 MTS/IEEE MARSEILLE, Marseille (FR)*. IEEE.

Gao, S., Hu, G., and Zhong, Y. (2015). Windowing and random weighting-based Adaptive Unscented Kalman Filter. *International Journal of Adaptive Control and Signal Processing*, 29(2), 201–223.

Hajiyev, C. and Soken, H.E. (2014). Robust adaptive Unscented Kalman Filter for attitude estimation of pico satellites. *International Journal of Adaptive Control and Signal Processing*, 28(2), 107–120.

Hurtós, N., Ribas, D., Cufí, X., Petillot, Y., and Salvi, J. (2015). Fourier-based registration for robust Forward-Looking SONAR mosaicing in low-visibility underwater environments. *Journal of Field Robotics*, 32(1), 123–151.

Jetto, L., Longhi, S., and Venturini, G. (1999). Development and experimental validation of an Adaptive Extended Kalman Filter for the localization of mobile robots. *IEEE Transactions on Robotics and Automation*, 15(2), 219–229.

Kalman, R.E. (1960). A new approach to linear filtering and prediction problems. *Journal of Basic Engineering*, 82(1), 35–45.

Mehra, R. (1972). Approaches to adaptive filtering. *IEEE Transactions on Automatic Control*, 17(5), 693–698.

Mehrjouyan, A. and Alfi, A. (2019). Robust Adaptive Unscented Kalman Filter for bearings-only tracking in three dimensional case. *Applied Ocean Research*, 87, 223–232.

Mohamed, A. and Schwarz, K. (1999). Adaptive Kalman filtering for INS/GPS. *Journal of Geodesy*, 73(4), 193–203.

Obsharsky, P., Schlee, F., and Toda, N. (1969). Region of Kalman filter convergence for several autonomous navigation modes. *AIAA Journal*, 7(4), 622–627.

Pfingsthorn, M., Birk, A., Schwertfeger, S., Bülow, H., and Pathak, K. (2010). Maximum likelihood mapping with spectral image registration. In *2010 IEEE International Conference on Robotics and Automation*, 4282–4287. IEEE.

Soken, H.E. and Hajiyev, C. (2012). UKF-based reconfigurable attitude parameters estimation and magnetometer calibration. *IEEE Transactions on Aerospace and Electronic Systems*, 48(3), 2614–2627.

Sun, F., Hu, X., Zou, Y., and Li, S. (2011). Adaptive Unscented Kalman filtering for state of charge estimation of a Lithium-Ion battery for electric vehicles. *Energy*, 36(5), 3531–3540.

Zheng, B., Fu, P., Li, B., and Yuan, X. (2018). A robust Adaptive Unscented Kalman Filter for nonlinear estimation with uncertain noise covariance. *Sensors*, 18(3), 808.

Zhu, H., Hu, H., and Gui, W. (2009). Adaptive Unscented Kalman Filter for deep-sea tracked vehicle localization. In *2009 International Conference on Information and Automation*, 1056–1061. IEEE.